V. Guidance and Control Research

GUIDANCE AND CONTROL DIVISION

A. Temperature Dependence of the Velocity of Sound in Liquid Helium; I. Theory, *W. M. Whitney*

1. Introduction

For liquid helium, there exists a microscopic model that can be used as a basis for calculating the temperature dependence of the entropy, specific heat, and other equilibrium properties; this is the phonon-roton model of Landau (Ref. 1), which was described briefly in an earlier report (SPS 37-39, Vol. IV, pp. 43–48). The velocity of sound at sufficiently low frequencies is an equilibrium property, and it should therefore be possible to determine its temperature dependence directly from the model. Since there is known to be good agreement between the calculated and measured temperature dependences of the thermal functions upon which the velocity depends, such a calculation would be of interest only as an exercise if it were not for the fact that the model itself is not complete. Its microscopic basis has not been fully worked out; in particular, the density dependence of four parameters that characterize the energy spectrum of the phonons and the rotons cannot be given in terms of basic quantities such as Planck's constant and the mass of the helium atom. Furthermore, experiments that have been done to date have not removed all doubt about what the density dependence of some of these parameters might be.

It will become clear from the present discussion that the temperature dependence of the sound velocity reflects certain relationships among the first and second derivatives of these parameters with respect to density. In this report, we will derive these relationships; in a later one, we will use them to analyze existing data (Ref. 2), including some measurements of the velocity at 10 MHz made recently in our laboratory. The calculations described below have been done in collaboration with C. E. Chase of the National Magnet Laboratory, M.I.T.

2. Hydrodynamic Considerations

It is known that liquid helium will sustain two kinds of wave motion: ordinary sound or pressure-density waves, arising from the elasticity of the fluid; and "second" sound, as it is called, which consists of the propagation of temperature and entropy fluctuations. The wave velocities for these two phenomena, at frequencies sufficiently low

that all dissipative effects can be ignored, are obtained from the hydrodynamic equations as roots of the following "compatibility" equation (Ref. 3):

$$(u^2 - V_1^2)(u^2 - V_2^2) = \frac{\gamma - 1}{\gamma} V_1^2 V_2^2, \qquad (1)$$

where

$$V_1^2 = (\partial p/\partial \rho)_S, \qquad V_2^2 = \frac{\rho_s}{\rho_n} \frac{T S^2}{C_v}.$$

In these expressions, T is the absolute (Kelvin) temperature, p is the pressure, S is the entropy per unit mass of fluid, and $\gamma = C_p/C_v$ is the ratio of the heat capacity per unit mass at constant pressure to that at constant volume. The normal fluid density ρ_n represents an effective mass associated with a heat flux, and can be calulated from the roton and phonon distribution functions. The superfluid density ρ_s is simply $\rho - \rho_n$.

In liquid helium, the difference $\gamma - 1$ does not exceed 2×10^{-3} at temperatures below 2°K, and is smaller than 10^{-4} over much of this region ($T < 1.3$°K). For this reason, the right-hand side of Eq. (1) is set equal to zero in the usual treatments. Note that for $\gamma = 1$, the two wave modes appear uncoupled and propagate with the velocities V_1 and V_2. In this approximation, the expressions for the velocity of "first" or ordinary sound are the same for liquid helium and for normal fluids. The fact that $\gamma \neq 1$ means that first and second sound are not entirely independent modes, and the coupling between them gives ordinary sound in liquid helium a slightly non-adiabatic character. The correction that arises in the expression for the velocity of ordinary sound when allowance is made for the coupling is small but not negligible. If we solve Eq. (1) for u_1, treating $(\gamma - 1)$ as a small quantity and ignoring terms of higher order, we obtain

$$u_1 = u_T \left[1 + \frac{\gamma - 1}{2} (1 - V_2^2/u_T^2)^{-1} \right].$$

To put the equation in the form shown, we have made use of the thermodynamic identity $(\partial p/\partial \rho)_s = \gamma (\partial p/\partial \rho)_T$ and have set $u_T = (\partial p/\partial \rho)_T^{1/2}$. We have also made the approximation

$$\gamma^{1/2} = [1 + (\gamma - 1)]^{1/2} \simeq 1 + \frac{1}{2}(\gamma - 1).$$

Sufficient accuracy is retained if, in the correction term, we replace u_T by u_{10}, the sound velocity at $T = 0$°K. We have finally

$$u_1 = u_T + \frac{1}{2}(\gamma - 1) u_{10} (1 - V_2^2/u_{10}^2)^{-1}. \qquad (2)$$

3. Thermodynamic Considerations

The pressure p can be written as a derivative of the Helmholtz free-energy function A (per unit mass of fluid):

$$p = \rho^2 (\partial A/\partial \rho)_T.$$

Since changes in the density are small over the temperature region of interest to us, we can expand p about the density ρ_0 at $T = 0$ to obtain

$$p = \rho_0^2 (\partial A/\partial \rho_0)_T + (\rho - \rho_0) \frac{\partial}{\partial \rho_0} \left(\rho_0^2 \frac{\partial A}{\partial \rho_0} \right)_T + \frac{1}{2}(\rho - \rho_0)^2 \frac{\partial^2}{\partial \rho_0^2} \left(\rho_0^2 \frac{\partial A}{\partial \rho_0} \right)_T + \cdots \qquad (3)$$

and

$$u_T^2 = (\partial p/\partial \rho)_T = \frac{\partial}{\partial \rho_0} \left(\rho_0^2 \frac{\partial A}{\partial \rho_0} \right)_T + (\rho - \rho_0) \frac{\partial^2}{\partial \rho_0^2} \left(\rho_0^2 \frac{\partial A}{\partial \rho_0} \right)_T + \cdots. \qquad (4)$$

Following similar treatments of anharmonic effects in elastic solids (Refs. 4, 5), we write the Helmholtz function as the sum of a zero-point energy U which depends only upon density, and a thermal energy F which is a function of both temperature and density and represents the free energy of the thermal excitations (the phonons and the rotons):

$$A(\rho, T) = U(\rho) + F(\rho, T).$$

It is assumed that $F << U$. At $T = 0$, where $F = 0$, $U(\rho_0)$ represents the minimum energy of the liquid, so $dU/d\rho_0 = 0$; consequently for $T \neq 0$,

$$(\partial A/\partial \rho_0)_T = (\partial F/\partial \rho_0)_T.$$

The velocity of sound when the fluid is in its ground state depends only upon U:

$$u_{10}^2 = \frac{d}{d\rho_0} \left(\rho_0^2 \frac{dU}{d\rho_0} \right) = \rho_0^2 \frac{d^2 U}{d\rho_0^2}.$$

When the substitutions indicated above have been made and terms of second order in the small quantities

$(\rho - \rho_0)$ and F have been dropped, Eqs. (3) and (4) take the forms

$$p = (\rho - \rho_0)\, u_{10}^2 + \rho_0^2 (\partial F / \partial \rho_0)_T , \tag{5}$$

$$u_T^2 = u_{10}^2 + 2(\rho - \rho_0)\, u_{10} \frac{du_{10}}{d\rho_0} + \frac{\partial}{\partial \rho_0}\left(\rho_0^2 \frac{\partial F}{\partial \rho_0}\right)_T . \tag{6}$$

Eq. (5) can be regarded as the equation of state for the liquid. Since the measurements with which the theory will be compared have been made under the saturated vapor pressure, we substitute the vapor pressure $P(T)$ for p in (5) and solve for the density:

$$\rho_{sat} - \rho_0 = P(T)/u_{10}^2 - (\rho_0^2/u_{10}^2)(\partial F/\partial \rho_0)_T .$$

After substituting this expression in (6) and taking the square root, remembering that the second and third terms on the right-hand side of that equation are small in comparison with the first, we obtain

$$u_T = u_{10} + \gamma_g \frac{P(T)}{\rho_0 u_{10}} + \frac{1}{2u_{10}} \times \left[\frac{\partial}{\partial \rho_0}\left(\rho_0^2 \frac{\partial F}{\partial \rho_0}\right)_T - 2\rho_0 \gamma_g \left(\frac{\partial F}{\partial \rho_0}\right)_T\right] \tag{7}$$

where $\gamma_g = (\rho_0/u_{10})\, du_{10}/d\rho_0$. Henceforth we drop the subscript zero from the density.

The contribution to u_T from the vapor pressure is of negligible importance (<0.1 cm/sec) below 1°K, but it increases rapidly with temperature and at 2°K amounts to 25 cm/sec.

4. The Phonon and Roton Contributions to the Velocity

The hydrodynamic and thermodynamic constraints on the behavior of the velocity are embodied in Eqs. (2) and (7). To proceed further, we must introduce explicit expressions for the thermal energy F. It is at this point that the phonon-roton model is invoked.

It can be assumed that all of the thermal energy of liquid helium below approximately 1.8°K is carried by two types of energy quanta—the phonons and the rotons, each type making a separate contribution to the thermal function F so that it is possible to write

$$F = F_{ph} + F_r .$$

To derive explicit formulas for F_{ph} and F_r from the model, one must know the relation between energy and momentum for each type of excitation. For the phonons, $\epsilon = cp$, where c is the phonon velocity. Inelastic neutron-scattering experiments (Ref. 6) show that, within experimental error, c is equal to the measured sound velocity at low frequency. In fact, this equality can be only approximate. The typical thermal phonon has a frequency $\nu = k_B T/h$ which amounts to ~20 GHz at 1°K, with a corresponding wavelength $\lambda \sim 120$ A. (k_B = Boltzmann's constant, h = Planck's constant.) The propagation of a phonon at such a frequency, for which the period is much shorter than the mean time between collisions of the phonons with each other or with rotons, is quite a different physical process from the low-frequency one that we are considering here. In making our numerical comparisons it will be expedient, and approximately correct, to set $c = u_{10}$, but for the moment we shall carry the phonon velocity along as a separate physical constant for liquid helium.

For rotons, $\epsilon = \Delta + (p - p_0)^2/2\mu$. Values of the three parameters Δ, p_0, and μ must be determined indirectly from measurements of the thermal properties of liquid helium, or directly from the dispersion curve $\epsilon(p)$-vs-p, which can be traced out in experiments with thermal neutrons (Ref. 6). From the results of both types of measurements carried out at different pressures, the derivatives of these quantities with respect to density can be estimated, although as mentioned previously the results of different experiments do not always agree.

From the dispersion relations given above, it can be shown that

$$F_{ph} = -\frac{\pi^2}{90}\frac{k_B T}{\rho}\left(\frac{k_B T}{\hbar c}\right)^3 ,$$

$$F_r = -\frac{2p_0^2 \mu^{1/2}}{(2\pi)^{3/2}\hbar^3 \rho}(k_B T)^{3/2} e^{-\Delta/k_B T} .$$

The velocity u_T can be represented by the sum

$$u_T = u_{10} + \delta u_{vp} + \delta u_{ph} + \delta u_r ,$$

where δu_{vp} denotes the vapor-pressure contribution. By taking the appropriate derivatives of F_{ph} and F_r, as required by Eq. (7), we obtain

$$\delta u_{ph} = G F_{ph}/u_{10}, \text{ where } G = 9\gamma_g^2 + \gamma_g - \frac{3}{2}\frac{\rho^2}{c}\left(\frac{\partial^2 c}{\partial \rho^2}\right)_T \tag{8}$$

[we have assumed that $(\rho/c)(\partial c/\partial\rho)_T \simeq \gamma_g$], and

$$\delta u_r = \frac{F_r}{2u_{1n}}\left[A + B(\Delta/k_BT) + C(\Delta/k_BT)^2\right], \qquad (9)$$

where

$$A = 2\gamma_g\left[1 - \left(\frac{\rho}{w}\frac{\partial w}{\partial\rho}\right)_T\right] + \left(\frac{\rho^2}{w}\frac{\partial^2 w}{\partial\rho^2}\right)_T,$$

$$B = 2\left(\frac{\rho}{\Delta}\frac{\partial\Delta}{\partial\rho}\right)_T\left[\gamma_g - \left(\frac{\rho}{w}\frac{\partial w}{\partial\rho}\right)_T\right] - \left(\frac{\rho^2\partial^2\Delta}{\Delta\,\partial\rho^2}\right)_T,$$

$$C = \left(\frac{\rho}{\Delta}\frac{\partial\Delta}{\partial\rho}\right)_T^2,$$

and

$$w = p_0^2/\mu^{1/2}.$$

The fact that both the first and second derivatives of the roton and phonon parameters appear in the expressions for δu_{ph} and δu_r means that it will not be possible to make separate determinations of these quantities by fitting experimental data to the theory. However, the values of the first derivatives can be estimated from other sources, so from these and the results of the fit the second derivatives can be calculated.

It should be emphasized that the results that we have obtained will be valid only at frequencies sufficiently low that the thermodynamic constraints remain in force; in particular, the period of the sound wave must always be small compared with the time required for thermal equilibrium to be established in the presence of the wave. Since the characteristic relaxation times increase rapidly as the temperature falls, the range above zero frequency over which the theory will be applicable will grow smaller and smaller as the temperature decreases. Generally speaking, measurements carried out at frequencies above 1 MHz cannot be compared with the theory at temperatures much below 1°K without making allowance for the frequency dependence of the velocity.

5. Behavior of the Velocity in the Phonon Region

Below 0.6°K, the rotons play a very minor role in sound propagation, and the temperature dependence of the velocity at zero frequency can be ascertained by considering the phonons alone. It is not difficult to show that the predicted low-temperature form of the equation for u_1 is

$$u_1 = u_{10} + u_{1n}\frac{\rho_{nph}}{\rho}\left\{\frac{1}{4}(3\gamma_g + 1)^2 - \frac{3}{2}\left[\gamma_g^2 - \frac{1}{4}\frac{\rho^2}{c}\left(\frac{\partial^2 c}{\partial\rho^2}\right)_1\right] - \frac{1}{4}\gamma_g(3\gamma_g + 1)\right\}, \qquad (10)$$

where

$$\rho_{nph}/\rho = \frac{2\pi^2}{45}\frac{k_BT}{\rho c^2}\left(\frac{k_BT}{\hbar c}\right)^3.$$

The first term inside the braces in Eq. (10) reflects the coupling between first and second sound and the factor γ that relates the isothermal and adiabatic compressibilities; the second term arises from the compressibility of the phonon gas; and the third term represents the change in velocity attributable to the shift in the zero-point energy $U(\rho)$ as the density changes. Corresponding expressions for the velocity at low frequencies in the phonon region have been given recently by Khalatnikov and Chernikova (Ref. 7) and by Disatnik (Ref. 8), whose approaches were quite different from that given here. They obtain an expression equivalent to Eq. (10) but with the last term left out. In both papers, no allowance has been made for the shift in zero-point energy. The numerical consequences of this omission are not negligible because the term that has been left out is comparable in magnitude (and identical in sign) with the sum of the terms left in. The treatments of Mott and Jones and of Landau and Lifshitz (Refs. 4 and 5) make it clear that the shift in zero-point energy cannot be ignored, so the expressions given by Khalatnikov and Chernikova and by Disatnik must be considered to be in error.

B. Boundary Trapping in Unipolar Space-Charge-Limited Current, *D. Stolfa, V. Rodriguez and M-A. Nicolet*[1]

1. Introduction

Within the limits of the approximations of Mott and Gurney, the flow of unipolar space-charge-limited current (sclc) at steady state follows the general law

$$I = \varepsilon\mu V^2/8 \qquad (1)$$

[1]At the California Institute of Technology, performing work supported by the Jet Propulsion Laboratory.

where V is the applied voltage, ϵ and μ are the dielectric constant and the mobility of the medium through which the current I passes, and δ is a factor which depends only on the geometrical configuration of the emitter and collector electrodes (Ref. 9). Values of δ are reported in the literature for the five distinct cases of the planar, cylindrical and spherical geometry (Ref. 10):

Planar

$$\delta = 9a\ 8W^3 \tag{1a}$$

Cylindrical

$$\delta = 2\pi l r_e^2\,[(k^2-1)^{1/2} - \arccos(k^{-1})]^{-2}, \qquad 1 \leq k \tag{1b}$$

$$\delta = 2\pi l r_e^2\,[\operatorname{arcosh}(k^{-1}) - (1-k^2)^{1/2}]^{-2}, \qquad k \leq 1 \tag{1c}$$

Spherical

$$\delta = 6\pi r_e^{-1}\left[\int_1^k (z^3-1)^{1/2} z^{-2}\,dz\right]^{-2}, \qquad 1 \leq k \tag{1d}$$

$$\delta = 6\pi r_e^{-1}\left[\int_k^1 (1-z^3)^{1/2} z^{-2}\,dz\right]^{-2}, \qquad k \leq 1 \tag{1e}$$

where, in the planar geometry, W is the width between emitter and collector boundaries, and a is the area under consideration. In the cylindrical geometry, r_e is the radius of the emitter, kr_e is the radius of the collector, and l is the length of the cylinder under consideration; r_e and k have the same meaning in the spherical geometry.[2]

Rose (Ref. 11) and Lampert (Refs. 12, 13) have shown that if the medium contains a uniform distribution of shallow traps—that is, traps whose population is in a Boltzmann equilibrium with the free charge carriers surrounding it—sclc is suppressed by a constant trapping factor $F << 1$. The modified characteristic

$$I = \epsilon\mu V^2 \delta F \tag{2}$$

is valid in a range $V << V_{TFL}$, a condition which reflects the assumption made in Eq. (2) that the space charge of the trapped charge carriers dominates and that the mobile charge carriers contribute negligibly to the divergence of the field.

[2]A confusion between $k = r_c/r_e$ and the Boltzmann constant is avoided if it is noticed that the latter appears only as a product kT, while the former never does.

It was shown recently (Ref. 10) that the value of the trapping factor F does not depend only on the energy distribution of the shallow traps, but that their spacial distribution also affects the value of F. In particular, shallow traps outside of the immediate neighborhood of the emitter are of little significance, except possibly for large peaks in the trap distribution. Since traps are most likely to occur in connection with imperfections, and since boundaries represent the most prominent imperfection of a lattice, trapping at the emitter boundary stands out as a particularly significant phenomenon. The purpose of this note is to discuss the properties and the significance of this effect.

2. Model for Boundary Trapping

Trapping at the emitter boundary will be described here by the most simple model, assuming that only one type of trap is present at the boundary in a surface concentration Σ and that the trap possesses one discrete trapping energy E_t in the forbidden band (see Fig. 1). A generalization including several discrete energy levels and/or trapping bands can be made along the lines developed in the analyses of bulk trapping and will not be considered here. It will be further assumed that $E_b - E_f$ is always at least several kT, so that Boltzmann statistics apply to the mobile charge carriers. No restriction will be imposed on the relative locations of E_t and E_f,

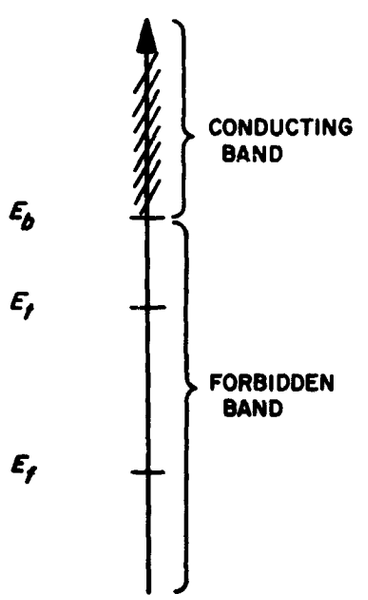

Fig. 1. The position of the energy level E_t of the trap is assumed to be known and fixed with respect to the band edge E_b; E_f shall not approach E_b by less than at least several kT

so that the population of the traps will have to be described by Fermi statistics. The trapped charge σ per unit area of the emitter boundary then is (q = value of electronic charge)

$$\sigma/q\Sigma = [(\exp(E_t - E_f)/kT) + 1]^{-1} \tag{3}$$

while the mobile charge carrier concentration ρ at the emitter is

$$\rho/qN = \exp[-(E_b - E_f)/kT] \tag{4}$$

where N is the effective density of states of the conducting band. Introducing $\gamma = \exp[(E_b - E_f)/kT]$ for E_f and $\beta = \exp[(E_b - E_t)\ kT]$ as a parameter one obtains

$$q\Sigma/\sigma = = \gamma\beta^{-1} + 1 \tag{3a}$$

and

$$qN/\rho = \gamma\,. \tag{4a}$$

The trapped charge will generate an electric field of a value $E = \sigma/\varepsilon$, and that same field will be responsible for the flow of current at the emitter boundary; hence, assuming that the field is constant on the emitter boundary,

$$I = a\mu\rho E = a\mu\rho\sigma/\varepsilon \tag{5}$$

where a is the total area of the emitter. Eqs. (3) to (5) specify ρ, σ and E_f or γ uniquely. The solution in terms of γ is

$$\gamma = (\beta/2)[-1 + (1 + 4b/\beta)^{1/2}] \tag{6}$$

which specifies the location of the Fermi level for any given trap depth and current via $\beta = \exp[(E_b - E_t)/kT]$ and

$$b = a\mu q^2 N\Sigma/I\varepsilon\,. \tag{7}$$

3. SCLC Dominated by Boundary Trapping ($V < V_{TFL}$ and $F << 1$)

In the limit of a "shallow"trap, that is, when the Fermi level lies below E_t by at least several kT, the population of the traps is governed by Boltzmann statistics as well and Eq. (6) simplifies to

$$\gamma = (\beta b)^{1/2} \tag{8}$$

which states that the mobile charge carrier concentration at the emitter varies as

$$\rho = (I\varepsilon N/a\mu\beta\Sigma)^{1/2} \tag{9}$$

while the ratio ρ/σ is constant

$$\rho = \sigma N/\beta\Sigma\,. \tag{10}$$

Since the current at the emitter boundary is $I = a\mu\rho E$ and ρ is given by Eq. (9), one obtains

$$I = (\varepsilon\mu a N/\beta\Sigma)\,E^2\,. \tag{11}$$

The voltage V, on the other hand, is determined solely by the field E since the space charge of the mobile charge carriers is negligible. One thus finds by direct integration

Planar $V = E \cdot W$ (12a)

Cylindrical $V = E \cdot r_e \ln(k)\,, \quad 1 \leq k$ (12b)

$V = E \cdot r_e \ln(k^{-1})\,, \quad k \leq 1$ (12c)

Spherical $V = E \cdot r_e(1 - k^{-1})\,, \quad 1 \leq k$ (12d)

$V = E \cdot r_e(k^{-1} - 1)\,, \quad k \leq 1\,.$ (12e)

All of these expressions are of the form

$$V = E\eta \tag{12}$$

where η depends on the geometry of the sample. The V-I characteristic therefore becomes

$$I = \varepsilon\mu V^2 \cdot a\eta^{-2} N/\beta\Sigma \tag{13}$$

and in agreement with Eq. (2).

In the limit where trapping dominates, the effect of boundary trapping at the emitter thus consists in introducing a factor $a\eta^{-2}N/\beta\Sigma$ into Eq. (1). Since $a\eta^{-2}$ depends on the geometry, this indicates that sclc will vary differently with the size of a structure depending on whether

trapping takes place uniformly in the volume or on the emitter boundary only, thus allowing us to distinguish between the two cases experimentally.

In the planar case, for example, shallow traps with a discrete energy level E_t and distributed uniformly throughout space at a density n_t will suppress sclc by a factor (Ref. 11):

$$F = N/\beta n_t \equiv \theta \tag{14}$$

for $V << V_{TFL}$, so that

$$I = \varepsilon\mu V^2 \cdot (9a/8W^3) \cdot \theta \tag{15}$$

while by Eq. (13) the same traps, when present at the emitter boundary only, will yield

$$I = \varepsilon\mu V^2 \cdot (a/W^2) \cdot (N/\beta\Sigma)\,. \tag{16}$$

This means that in this case F has a value of $8WN/9\beta\Sigma$, which may be written as

$$F = (8/9)\,\theta_{eff} \tag{17}$$

where

$$\theta_{eff} = WN/\beta\Sigma \tag{18}$$

has a form identical to that occurring in Eq. (14). The main difference between Eqs. (15) and (16) is in the thickness dependence of the current. For volume trapping F is constant and $I \simeq W^{-3}$, while for boundary trapping at the emitter F is proportional to W and $I \simeq W^{-2}$.

A comparison of the same two cases in cylindrical geometry readily shows that for volume trapping

$$I = \varepsilon\mu V^2 \cdot 2\pi l r_e^{-2} \times [(k^2-1)^{1/2} - \arccos(k^{-1})]^{-2} \cdot \theta\,, \qquad 1 \leq k \tag{19}$$

while for boundary trapping at the emitter

$$I = \varepsilon\mu V^2 \cdot 2\pi l r_e^{-1} ln^{-2}(k) \cdot N/\beta\Sigma\,, \qquad 1 \leq k\,. \tag{20}$$

In this case also the dependence on the geometrical scaling factor r_e is reduced by one order for boundary trapping. For the last expression F now has the value

$$F = \left(\frac{[(k^2-1)^{1/2} - \arccos(k^{-1})]}{ln(k)}\right)^2 \cdot \theta_{eff} \tag{21}$$

where

$$\theta_{eff} = r_e N/\beta\Sigma\,. \tag{22}$$

Analogous hold for $k \leq 1$.

A similar comparison in spherical geometry leads to a remarkable fact. For volume trapping

$$I = \varepsilon\mu V^2 \cdot 6\pi r_e^{-1}\left[\int_1^k (z^3-1)^{1/2} z^{-2} dz\right]^{-2} \cdot \theta\,, \qquad 1 \leq k \tag{23}$$

but for boundary trapping at the emitter

$$I = \varepsilon\mu V^2 \cdot 4\pi\,(1-k^{-1})^{-2} \cdot N/\beta\Sigma\,, \qquad 1 \leq k\,. \tag{24}$$

Again, the dependence on r_e has been reduced by one order. The current I is now *independent* of the scaling factor r_e. Since the variation with k disappears also for $k >> 1$, *unipolar sclc dominated by boundary trapping is essentially independent on sample dimension in spherical geometry and* $r_c >> r_e$. This property, combined with the experimental significance of the point contact, may offer new possibilities in the study of sclc or the evaluation of material parameters such as μ, N or Σ because it does not require accurate control or even the knowledge of sample dimensions. It should be noted, however, that this result holds only for $1 << k$. For $k << 1$ Eq. (24) contains an additional factor k^2 which reintroduces a geometrical factor into the equation.

The absence of r_e in Eq. (24) is due to a combination of mutually independent effects. The following arguments will help to reveal their origin. At the emitter, the current density is given by $j = \mu\rho E$. The model is such that with the knowledge of E the applied voltage is also determined by direct integration over the same field E; hence, $V = Er_e(1-k^{-1})$. This expression is independent of k for $k >> 1$ because the field decreases so rapidly for $r_c >> r_e$ in the spherical geometry that the overall potential is determined essentially by the field distribution in the vicinity of the emitter only. This explains the independence of the current on the geometrical factor k and establishes that $E \simeq V/r_e$. But E also specifies the surface density of the trapped charge $\sigma = \varepsilon E$ and through it the

free charge carrier concentration $\rho = \sigma(N/\beta\Sigma)$, so that the current density j is proportional to E^2. The current is thus $I = 4\pi r_c^2 \cdot j \simeq 4\pi r_c^2 \cdot V^2/r_c^2$. For fixed applied voltage V, a change in emitter radius thus generates a variation in $E \cdot \rho$ which exactly cancels the effect of the changing emitter area.

The results derived in this section are summarized in Table 1. The voltage V_{TFL} which sets an upper limit for the validity of these results is also given. It is found by assuming in Eq. (12) that all traps are filled, that is, by setting $E = q\Sigma/\varepsilon$.

4. Complete V-I Characteristic

The preceding considerations are limited to the range $V << V_{TFL}$ by the assumption that Boltzmann statistics governs the population of the traps. For a general discussion, Fermi statistics has to be used and Eq. (8) must be replaced by the more general relation (6). The ratio of ρ/σ is no longer constant and the analysis becomes more tedious. The space charge of the mobile carriers is no longer negligible either. The solution must now be obtained by a formal integration of the set of equations

$$\nabla \cdot \varepsilon \mathbf{E} = \rho$$

$$\nabla \cdot \mathbf{j} = 0 \qquad (25)$$

$$\mathbf{j} = \mu\rho\mathbf{E}$$

which may be combined into a single differential equation

$$\nabla \cdot (\mathbf{E}\nabla \cdot \mathbf{E}) = 0. \qquad (26)$$

The boundary conditions are as discussed in Sect. 2. The analysis can be carried out explicitly for both the planar and the cylindrical geometry, while numerical integrations are required in the spherical geometry. Fig. 2 shows the result for the planar case. Voltage is normalized with respect to $V_{TFL} = q\Sigma W/\varepsilon$ and current is given in units of the current $I_{TFL} = \varepsilon\mu V_{TFL}^2(9a/8W^3)$ which would flow in the absence of traps at a bias V_{TFL}. As expected, the characteristic follows a square law for $V << V_{TFL}$ and F has the constant value $(8/9)(WN/\beta\Sigma)$ given in Table 1.

The main feature of Fig. 2 is the rapid increase in current in the vicinity of V_{TFL}. This reflects the fact that the traps are being all filled at this point ($E_f \simeq E_t$). Beyond this, sclc is rapidly approaching its trap-free limit $\bar{I} \simeq \bar{V}^2$. The overall characteristic is in all respects similar to that

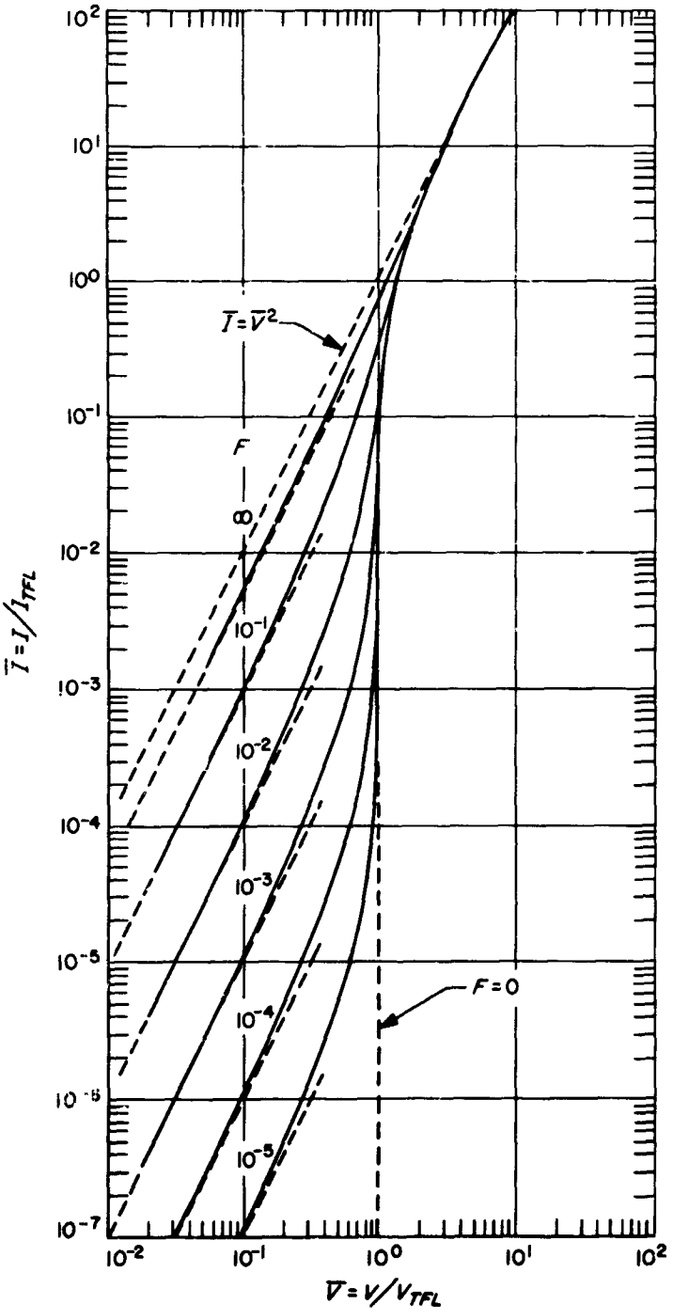

Fig. 2. Complete V-I characteristic of unipolar sclc in the presence of traps at the emitter boundary and for a planar configuration ($V_{TFL} = q\Sigma W/\varepsilon$; $I_{TFL} = \varepsilon\mu V_{TFL}^2(9a/8W^3)$; $F = 8WN/9\beta\Sigma$)

predicted by volume trapping (Refs. 11, 12), but in this latter case $F = \theta$ is independent of the base width W.

5. Discussion and Conclusion

The effect of volume trapping on the V-I characteristic of sclc at steady state is indistinguishable from that of

Table 1. The *V-I* characteristic of unipolar sclc dominated by boundary trapping at the emitter ($V << V_{TFL}$ and $F << 1$) for the five distinct cases of the planar, cylindrical and spherical geometry

Geometry	$0 \leqq k = \frac{r_c}{r_e}$	I	or	$I = \varepsilon\mu V^2 \delta F \, (F << 1)$	V_{TFL}
Planar		$\varepsilon\mu V^2 \cdot \frac{a}{W} \cdot \frac{N}{\beta\Sigma}$		$F = \frac{8}{9} \cdot \frac{WN}{\beta\Sigma}$	$\frac{q\Sigma}{\varepsilon} \cdot W$
Cylindrical	$1 \leqq k$	$\varepsilon\mu V^2 \cdot \frac{2\pi l}{r_e ln^2(k)} \cdot \frac{N}{\beta\Sigma}$		$F = \left[\frac{(k^2-1)^{1/2} - \arccos(k^{-1})}{ln(k)}\right]^2 \cdot \frac{r_e N}{\beta\Sigma}$	$\frac{q\Sigma}{\varepsilon} \cdot r_e ln(k)$
	$k \leqq 1$	$\varepsilon\mu V^2 \cdot \frac{2\pi l}{r_e ln^2(k^{-1})} \cdot \frac{N}{\beta\Sigma}$		$F = \left[\frac{\operatorname{arcosh}(k^{-1}) - (1-k^2)^{1/2}}{ln(k^{-1})}\right]^2 \cdot \frac{r_e N}{\beta\Sigma}$	$\frac{q\Sigma}{\varepsilon} \cdot r_e ln(k^{-1})$
Spherical	$1 \leqq k$	$\varepsilon\mu V^2 \cdot \frac{4\pi}{(1-k^{-1})^2} \cdot \frac{N}{\beta\Sigma}$		$F = \frac{4}{6}\left[\frac{\int_1^k (z^3-1)^{1/2} z^{-2} dz}{1-k^{-1}}\right]^2 \cdot \frac{r_e N}{\beta\Sigma}$	$\frac{q\Sigma}{\varepsilon} \cdot r_e (1-k^{-1})$
	$k \leqq 1$	$\varepsilon\mu V^2 \cdot \frac{4\pi}{(k^{-1}-1)^2} \cdot \frac{N}{\beta\Sigma}$		$F = \frac{4}{6}\left[\frac{\int_k^1 (1-z^3)^{1/2} z^{-2} dz}{k^{-1}-1}\right]^2 \cdot \frac{r_e N}{\beta\Sigma}$	$\frac{q\Sigma}{\varepsilon} \cdot r_e (k^{-1}-1)$

boundary trapping at the emitter. This fact corroborates the conclusion reached in Ref. 10 whereby a measurement of the V-I characteristic of sclc in a device is insufficient to specify the nature of the traps, if trapping is observed. Additional information is therefore essential if interpretations are to have more than a merely suggestive character. Such information can be obtained from measurements of the V-I characteristics on a set of comparable devices of different sizes and geometries. The present note demonstrates that the two limiting cases of uniform trapping throughout the base without boundary trapping and boundary trapping at the emitter without volume trapping can readily be distinguished in this manner. Mixtures of both types of trapping in the same device will of course lead to intermediary results. To clarify more complicated systems such as these then also demands more sophisticated experimental studies.

Only few investigators have given this problem the attention it deserves. There are, correspondingly, only a few experiments reported in the literature in which samples of various geometries but otherwise identical features have been produced and studied. Where trapping is observed in this fashion, the evidence points towards volume trapping.

An independent check on the nature of the trapping is offered by V_{TFL} if this quantity is experimentally accessible. Volume and boundary trapping each predict a specific dependence of V_{TFL} on the geometrical scaling factor W or r_e. It is invariably assumed in the literature that volume trapping is present when a threshold V_{TFL} is reported. Experimental observations of V_{TFL} are not numerous, and its thickness dependence is studied rarely. The evidence, again, seems to favor volume trapping.

In summary it can be stated that most of the observations reported in the literature and interpreted in terms of trapping in the bulk can readily be re-interpreted in terms of boundary trapping at the emitter or, more generally, in terms of any arbitrary distribution of traps in space. Insight into the nature of the traps can be gained from changes observed in V_{TFL} and in the characteristic of sclc below V_{TFL} as the size and geometry of the sample is varied. Such measurements have been performed very infrequently. The two idealized models of pure volume trapping and pure boundary trapping thus offer equally simple alternatives of interpretation. In view of some remarkable consequences predicted for boundary trapping on point contacts, an experimental clarification of the actual location of traps and their distribution in space is most desirable.

C. Applications of Superconductivity in Spacecraft, *P. V. Mason*

1. Introduction

The properties of superconductors which appear to be of engineering interest include: (1) zero dc resistance, (2) flux exclusion, (3) switching to the normal state induced by temperature, by applied magnetic field, and by self current, (4) quantization of flux, and (5) tunneling currents between superconductors, both single particle and Josephson.

In judging applications of superconductivity, we have used the following criteria: First, the time scale for final application can be long range—say up to 10 yr; we assume that larger weight and power limits and much more complex missions will prevail. Second, the size and weight of refrigeration will be relatively large, certainly not less than 100 lb and several hundred kilowatts for systems that must be operated continuously; for short-term operation such as a planetary encounter this can be considerably reduced.

Thus the payoff must be large; the application must either be a function that can be done in no other way, or a large number of tasks must be performed more efficiently than can be done otherwise. If the application is a short-term one, with very low heat loads, this requirement may be relaxed. The applications may be divided into the following categories:

a. Active and signal-handling devices. These include (1) switching devices such as cryotrons and related devices, (2) linear amplifiers, and (3) parametric amplifiers.

b. Memories. Superconductors may serve in (1) random access memories, and (2) associative memories.

c. High-field solenoids. These may be used in (1) spacecraft shielding, and in (2) fields for masers and other devices.

d. High-Q circuits and transmission lines. Superconductivity may be applied to (1) selective circuits, and (2) data transmission and compression devices.

e. Power generation and handling. These include (1) generators, (2) converters, and (3) energy storage devices.

f. Sensors. Improved performance may be obtained with (1) magnetometers, (2) infrared detectors, (3) gyroscopes and accelerometers, (4) voltage to frequency conversion and vice-versa, and (5) alpha particle detectors.

g. Propulsion.

In this summary, we will discuss only items a, b, and c, above. The remainder will appear in later issues.

2. Active Devices

A number of successful devices have been built around the superconducting-to-normal transition induced by the magnetic field of a current-carrying wire or film. Such systems are usually in thin-film form in order to reduce inductance and increase normal resistance, since the major factor determining speed is the ratio of the inductance to normal resistance.

As usually seems to be the case in integrated circuit devices, which these closely resemble in physical form, switching devices have been most successful, while linear amplifiers have followed relatively slowly. Packing densities of 10^4 devices/in.^{2} of substrate and perhaps 10^5 to 2×10^5/in.^{3} of refrigerated space are now possible; perhaps 10^6/in.^{2} and 10^7 to 10^8/in.^{3} is possible in the future.

Speeds are now in the sub-microsecond range, and increases to the 10-nanosec range seem possible. Impedances are typically in the milliohm range, so voltages are characteristically of the order of microvolts to millivolts, and currents of the order of tens of milliamperes.

In order to raise the voltage level, various linear amplifiers have been developed. The principal problem is that of obtaining high gain and short time constant simultaneously or, to put it another way, a good gain bandwidth product. Principal advantage is high sensitivity. A recently developed device has a sensitivity of 2×10^{-13} volts and a bandwidth of 750 kHz.

In another direction, a family of parametric microwave amplifiers based on the nonlinear properties of thin films has been developed. Typical figures are 27 db gain at 2 GHz and 6 db at 54 GHz. However, power outputs are in the microwatt range.

A promising development is in the area of a family of devices—diodes and triodes—based on the Josephson effect. Very preliminary measurements have shown switching speeds in the sub-nanosecond range.

The advantages of cryotron devices lie in their high density, moderate speed, low heat dissipation and (presumably) high reliability. Their disadvantages, aside from the obvious ones connected with refrigeration, lie in the decrease in speed with number of cascaded elements, low impedances and voltage levels, and difficulties of interconnection between substrate planes. Over-all, it does not seem that the advantages are enough to justify the cost for spacecraft applications. However, if some other device, for example, a cryoelectric memory or magnetometer were required, then the use of cryotrons may be justified.

The Josephson devices, if they fulfill their promise, may be useful as the need for sophisticated high-speed computing increases.

In addition, active devices will be necessary as components of the cryoelectric memory described below; hence a study of them will be needed if cryoelectric memories are to be developed.

3. Cryoelectric Memories

One of the most promising areas of application of superconductors is the large-scale random-access and associative memories. Cryoelectric memories are based on the following effects; first, that current circulating in a superconducting ring will flow indefinitely, and second, that it can be destroyed by making part of the ring normal by generating magnetic field by passing current through a nearby wire. Currents can be excited in either direction by suitable timing of an applied current and a switching current. Readout is made by noting the voltage generated in a sense line when the current is destroyed.

Thus, all elements of a memory rather similar to the conventional magnetic core memory are available. As in the cryotron, best performance is obtained when the device is formed of thin films. Hence batch fabrication is both easy and desirable. Densities for simple random access cells are similar to those for cryotrons. A 10^8 bit random access memory in 1 ft^3 of refrigerated volume is now being built, and 10^9 bit appears well within reach.

Advantages of cryoelectric memories are: high storage density, zero power dissipation while holding a bit, batch fabrication and high speed. Individual cells can be switched in 5 to 25 nanosec, although cycle times are about a microsecond because of delays in the cryotron selection trees which select an individual bit. Disadvantages are: tolerances and yields in fabrication, difficulties in low impedance interconnections between substrate planes, and low voltage outputs—typically 20 μv. The latter is alleviated by the fact that the signal-to-noise ratio is good, so that transformers or active amplifiers can be used to raise the level.

Another attractive possibility lies in the flexibility which the fabrication process allows for incorporating logic into the individual memory cells. At the cost of increased area per cell, a wide variety of functions can be performed. The basic function is a comparison of the cell contents with an external signal, yielding an agree/disagree or a less-than/equal/greater-than/output. One form this takes is an associative or content-addressed memory. A word held in an external register can be compared with part or all of all words in memory and a positive output obtained if one of the words is the same. Then the matched word can be read out. There have also been proposals to perform arithmetic operations in the memory.

Over-all, the cryoelectric memory seems to be the most likely candidate for spacecraft applications such as data compression, where very large amounts of data must be handled and stored.

4. High-Field Magnets

Certain alloy superconductors can carry currents of up to 10^6 amp/cm^2 at zero field, and 3×10^5 amp/cm^2 at 100 kilogauss with no voltage drop. Thus, high-field large-volume magnets can be made that require no steady-state energy input. Solenoids as large as 1 ft bore by 10 ft long with a field of 40 kilogauss are under construction for use on plasma power-generation experiments. A Helmholtz pair 14 ft in diameter with a 2-ft separation, and a field of 30 kg, is being designed for a hydrogen bubble-chamber application at Brookhaven National Laboratory.

The economics strongly favors superconductors in such applications because the refrigeration is much cheaper than the large amounts of power required for conventional coils.

The most direct application so far suggested for high field coils in spacecraft is a scheme to shield manned spacecraft from high energy particles. The spacecraft is charged to a high positive voltage to repel positively charged particles and the magnetic field deflects the negative particles. The field required is about 2500 gauss over the entire protected volume. Such a system would be prohibitively heavy if done with normal conductors, but would weigh in the vicinity of 1000 to 2000 lb if done with superconductors.

Other possible applications include providing fields for devices which already require cooling such as masers. Also if plasma devices are used to provide power, high magnetic fields could be efficiently generated by superconducting magnets.

D. Enhanced Electron Emission in Plasma Mode,

K. Shimada and S. Luebbers

1. Introduction

An experimental study of a thermionic-energy converter which utilizes an applied axial magnetic field has been initiated. The objective of this study is to investigate the possibility of increasing the output voltage of a thermionic converter by increasing the ionization efficiency. Such an increase would reduce the plasma-sustaining voltage. A test converter having an interelectrode gap of 28 mils was designed and fabricated by the Thermo-Electron Engineering Company (TEECo), Boston, Massachusetts. This diode differs from conventional thermionic converters which have been tested at JPL with regard to: (1) the interelectrode gap, which is nearly 10 times larger, and (2) the emitter side walls, which are kept at the same temperature as the planar part of the emitter.

The experimental diode is operated at considerably lower cesium pressures and emitter temperatures than conventional thermionic converters. Such a mode of operation is chosen to minimize internal losses due to electron scattering by cesium atoms. During operation of the experimental converter, with no applied magnetic field, the observed currents were two or three orders of magnitude greater than normally anticipated. In addition, the diode would go into a self-sustained discharge which is indicative of positive-ion bombardment of the emitter. Heat balance experiments were performed to allow separation of electron and ion-current effects and to give a better understanding of the phenomena involved.

To give assurance of credibility to the observed high currents, a conventional converter was tested. Once again, anomalously high currents resulted under similar temperature conditions. The conventional converter has a nominal interelectrode spacing of 0.002 in., and minimizes emitter-side-wall emission. As would be expected from similarity considerations, the conventional converter (closely-spaced) required a higher cesium pressure to maintain a constant pressure-spacing product.

2. Converter Characteristics

Before describing our experiments, we briefly describe the characteristics of conventional thermionic-energy converters.

The charge transport in thermionic converters may be understood by considering two planar electrodes separated from each other by an interelectrode gap *d*. The

emitter electrode is operated at elevated temperatures to utilize thermionic emission, and the collector is operated at a lower temperature to provide "contact potential" between the electrodes. The cesium vapor present in the interelectrode gap serves to modify the electrode work functions (Ref. 14); when ionized, the cesium reduces the effect of negative space charge within the interelectrode gap. Fig. 3 is a schematic representation of a thermionic converter. The interelectrode gap is grossly exaggerated for clarity and is nominally 0.002 to 0.030 in.

When the converter is operated at high emitter temperatures ($T_E \simeq 2000°K$) and at large cesium pressures ($pd > 10$ mil-torr), volt-ampere curves such as those shown in Fig. 4 are obtained. However, if the emitter temperature and pd are reduced, another volt-ampere curve, which is also shown in Fig. 4, results. In the latter curve, two fundamental modes, the unignited mode (ABC) and the ignited mode (DEF), are indicated. In contrast to this case, at high emitter temperatures no clear change in mode is evident, and the entire region may be considered as the ignited mode.

An essential difference between these modes lies in the fact that volume ionization of cesium exists in the ignited mode, whereas surface ionization is the dominant process of ion generation in the unignited mode. Corresponding motive diagrams, which are the energy diagrams for electrons, are shown in Fig. 5. The region AB (in Fig. 4) is the Boltzmann region where the current depends exponentially on the applied voltage, since the motive diagram is strongly electron-retarding. The region BC is a quasi-saturation region where the current is much less than the temperature-saturated emission current from the emitter. The saturation current is reduced by an exponential factor $\exp(-e\Delta V/kT_E)$, where ΔV is the height of the electron potential in excess of the emitter work function Φ_E. In the region BC, ΔV remains relatively unchanged as the output voltage is varied. As the voltage across the diode is further reduced, the motive diagram becomes more electron-accelerating, and inelastic collisions between thermionically emitted electrons and cesium neutrals cause cesium ionization. The generation of cesium ions results in a reduction of the aforementioned ΔV, and high currents are obtained. Operation in the ignited mode is accompanied by a plasma-sustaining voltage drop, V_d, of the order of 0.5 v. At a point E, which is a knee of the volt-ampere curve, the electron-retarding sheath near

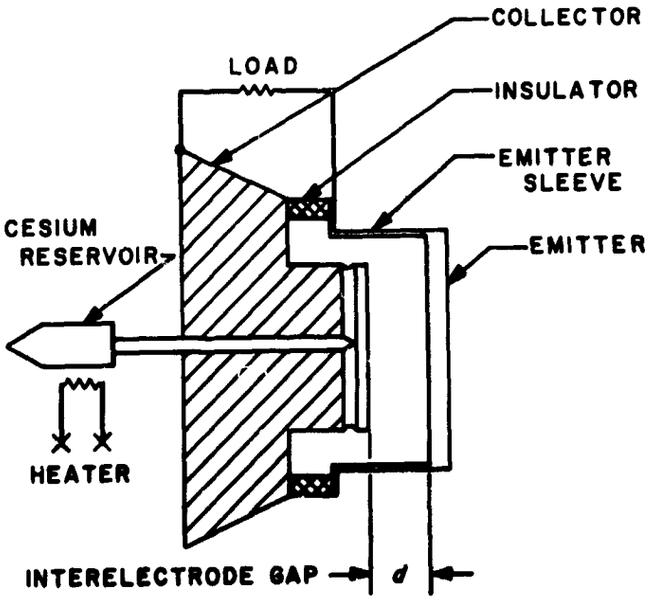

Fig. 3. Schematic representation of a planar thermionic converter

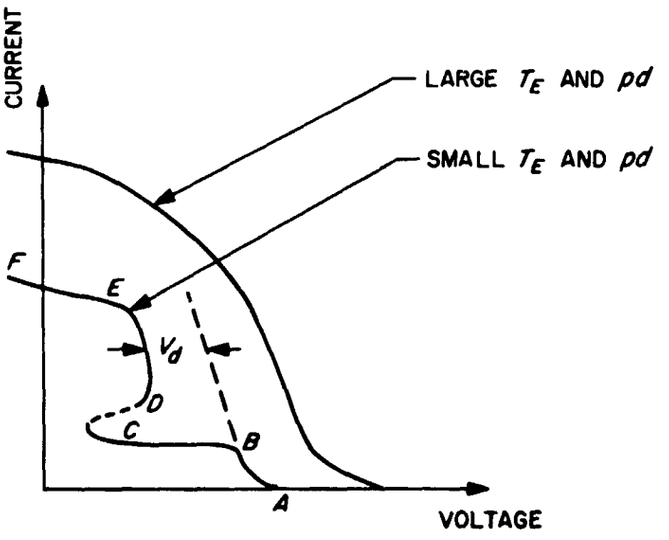

Fig. 4. Converter volt-ampere characteristics illustrating the different modes of operation

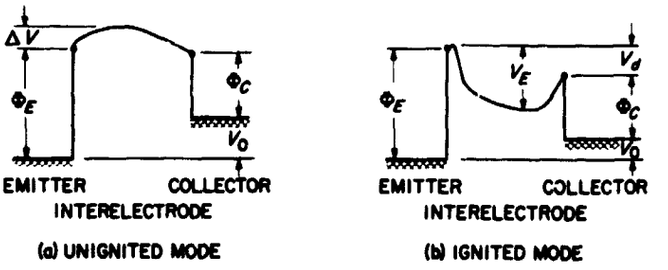

Fig. 5. Motive diagrams illustrating electron potential energy within a thermionic converter

the emitter vanishes. Therefore, the current again saturates near a value equal to the temperature-saturated emission current but is reduced due to electron scattering in the interelectrode space. In the region EF, electron scattering and Schottky enhancement modify the current.

The cesium diode tested in our laboratory operates with a low emitter temperature and in a regime where the pressure-spacing product (pd) is less than unity. These conditions produce relatively small currents in the power-producing quadrant; however, as voltage is applied to the diode an anomalous ignition is observed and the current "soars" to a value two to three orders of magnitude higher than anticipated from normal saturation current. To distinguish this high-current operation from the normal ignited mode, we shall refer to it as the plasma mode. Observed characteristics in the plasma mode are discussed in the subsequent sections.

3. Experiment

External emitter-heating power was supplied by electron bombardment from a Pierce gun (SPS 37-41, Vol. IV, p. 46), designed and fabricated by JPL. Utilization of an electron gun, displaced from the emitter by 10 cm or more, permits calculation of heat input power to the emitter without inclusion of radiation-heating by the gun filament. The bombardment voltage and current were both accurately measured on a digital voltmeter. The emitter temperature was observed in a "hohlraum" using a Mikro-Werk pyrometer. All other temperature monitoring was provided by uninterrupted Chromel-Alumel thermocouples.

The tests performed on both the experimental and conventional converter included: volt-ampere performance characteristics, electrode work-function measurements, and emitter heat balance. The latter experiments provide the necessary information for calculation of ion current and emitter work function in the plasma mode. The heat balance results strongly suggest we look for an unconventional explanation of the work-function adjustment in the presence of a highly ionized cesium plasma or electron emission resulting from some secondary mechanism. The remainder of this paper will be confined primarily to heat balance experiments and discussion of the observed plasma mode.

4. Results

The semi-log representation of the volt-ampere curve shown in Fig. 6 was obtained from the experimental converter. The applied voltage is shown on the abscissa and

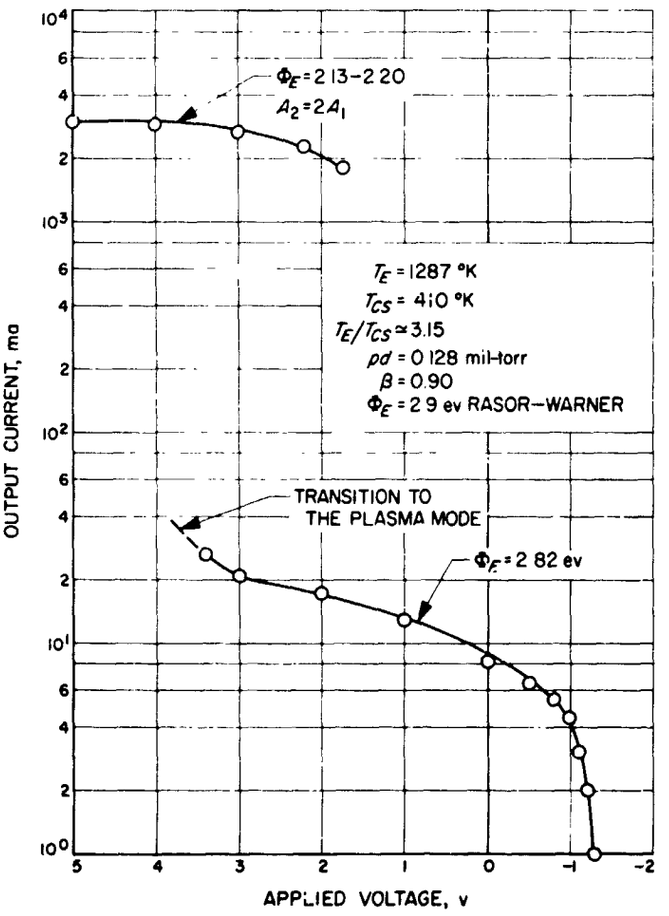

Fig. 6. Volt-ampere characteristics at T_E = 1287°K

spans the range of +5 to −2 v. The power generation quadrant (negative voltage) is seen to contain the linear Boltzmann behavior and a gently sloping saturation due to Schottky effects. As the voltage across the diode approaches the ionization potential of cesium (3.89 v), the current continues the slow rise and suddenly makes the transition into the plasma mode. The lower portion of the curve is the anticipated behavior discussed in Sect. 2, "Converter Characteristics." In this lower region, the converter is temperature-saturated as long as the diode operates in an ion-rich mode. If the current at zero volts is considered to be the saturated current value, the emitter work function calculated from the Richardson equation is 2.82 eV. This is in reasonable agreement with the theoretical value of 2.9 eV determined from a Φ_E-versus-T_E/T_{cs} plot for an emitter with a bare-work function of 4.5 eV. On the other hand, the saturation current value observed in the plasma mode would require an emitter work function of 2.15 eV for thermionic saturation. This is in strong disagreement with known behavior of refractory emitters in contact with cesium vapor. It

should be noted that the curve in Fig. 6 is a semi-log plot and the discontinuity in current spans two decades.

Volt-ampere curves of the converter operating in the plasma mode for various cesium reservoir temperatures are shown in Fig. 7. Power input measurements at each data point in the figure permit the distinction to be made between electron and ion currents. This distinction is apparent from a plot of the additional heating power required to maintain a constant emitter temperature for varying applied voltages. For voltages greater than 1 v, the current approaches saturation. This means that the electron current as well as the ion current reaches saturation. Consequently, the electron cooling of the emitter remains constant as the applied voltage is increased, whereas the energy returned to the emitter from the plasma increases as the applied voltage is increased. Ions impinging on the emitter not only transfer their kinetic energy but also give energies to the emitter as they recombine (Ref. 15). The energy returned from the plasma by excited cesium atoms and by photons is considered to be negligible compared with the energy returned by ions.

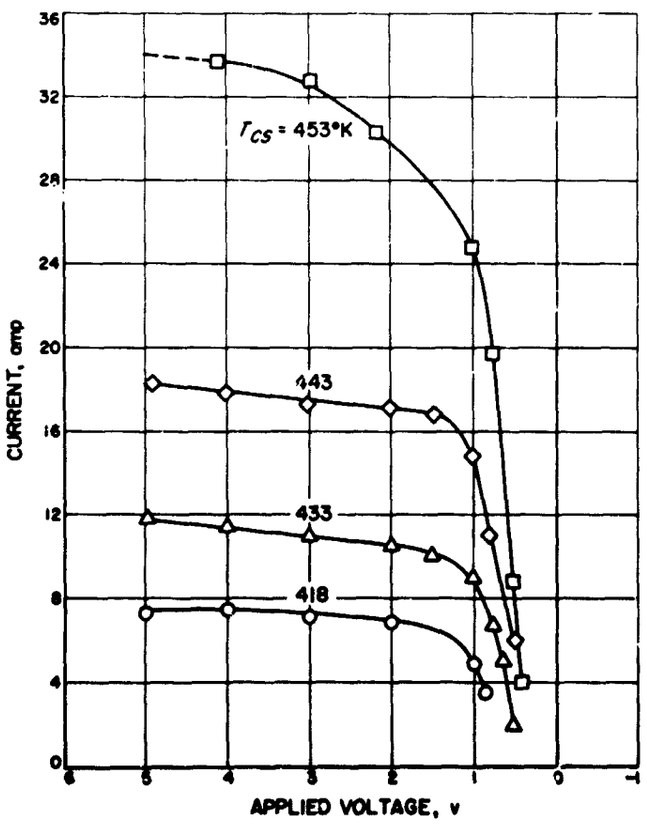

Fig. 7. Volt-ampere characteristics in plasma mode

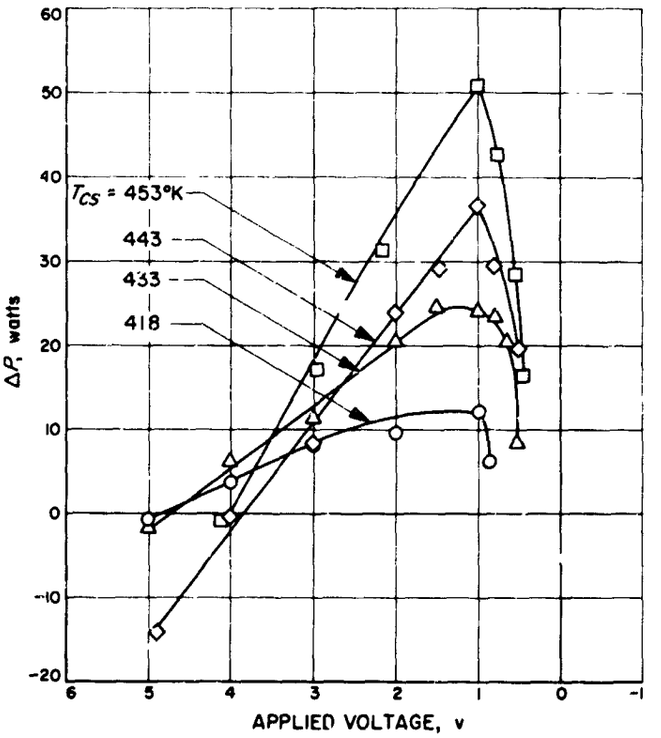

Fig. 8. ΔP versus applied voltage $T_E = 1190°K$

If the emitter sheath voltage V_E, which has a polarity to accelerate ions flowing out of the plasma to the emitter, varies linearly with the applied voltage, we would expect a corresponding linear decrease in the input power ΔP as the applied voltage is increased. This behavior is exhibited in Fig. 8 for applied voltages in excess of 2.0 v. The slope of the linear region yields the value of the saturated ion current. The results for the four curves shown in Fig. 8 are tabulated in Table 2. In all four curves we see that the ion current is comparable with the electron current.

Table 2. Saturated ion and electron currents

T_{CS}, °K	I_+, amp	I_-, amp	I_{net}, amp
418	7.5	3.0	4.5
433	12.0	4.6	7.4
443	18.0	5.3	12.7
453	34.0	16.0	18.0

Subtraction of the ion current from the net current yields the forward electron current. Using this reduced current to determine Φ_E from the Richardson equation, we calculate the values of Φ_E and tabulate them in Table 3. Also shown are the conventional work function values

Table 3. Comparison of emitter work function values

T_{cs}, °K	Φ_E Calculate from Richardson Eq. (experimental)	Φ_E From Φ_E versus T/T_{cs} plot
418	1.94	2.55
433	1.90	2.45
443	1.87	2.35
453	1.77	2.27

anticipated from a Φ_E versus T/T_{cs} plot. We see marked disagreement between the calculated and anticipated values.

5. Conclusions

If the electron currents tabulated in Table 2 originate from thermionic emission, the emitter work function values calculated from the Richardson equation (column 2 of Table 3) must be correct. An obvious difference between the plasma mode and the ignited mode is the fact that the ion current arriving at the emitter in the plasma mode is many times larger than ordinarily encountered. In other words, the theory for the work function of cesiated surfaces, which is based upon the arrival rate of cesium neutrals and not of cesium ions, may have to be modified to be applicable to the plasma mode. In fact, the degree of ionization appears to be near 100% in the plasma mode, while it is a small fraction in conventional thermionic energy converters operating in the ignited mode.

The presence of a large ion arrival rate at the emitter admits the possibility of other secondary electron-emission processes. The higher ion concentration at the emitter will produce large changes in potential (see Fig. 5b) adjacent to the emitter and, hence, high-field or Schottky enhancement seems possible. A calculation of the field strength at the emitter required to produce the enhancement present in the plasma mode quickly discounts both of these possibilities. Schottky enhancement could account for an increase in current by a factor of 3, while field emission effects are negligible. Neither of these secondary mechanisms explains the observed increase in current. Auger emission is also being considered as a possible secondary mechanism; however, at this time, no concrete conclusion may be drawn.

The dependence of the emitter work function upon the ion arrival rate and the possibility of Auger emission are both under investigation. These investigations are to be conducted in a guard-ringed test vehicle to minimize extraneous emission from undefined electrode surfaces. In addition, a glass tube is being fabricated which will permit visual observation of the discharge.

It is hoped that a suitable explanation of the plasma mode will result from these tests.

References

1. Landau, L. D., *J. Phys.* (Moscow), Vol. 5: p. 71, 1941; Vol. 11: p. 91, 1947.
2. Whitney, W. M., and Chase, C. E., to be published in *Physical Review*.
3. Atkins, K. R., *Liquid Helium*, Chap. 5, Cambridge University Press, 1959.
4. Mott, N. F., and Jones, H., *The Theory of the Properties of Metals and Alloys*, p. 15ff., Dover Publications, Inc., New York, 1958.
5. Landau, L. D., and Lifshitz, E. M., *Statistical Physics*, pp. 180–184, Pergamon Press, Ltd., London, 1958.
6. Yarnell, J. L., Arnold, G. P., Bendt, P. J., and Kerr, E. C., *Physical Review*, Vol. 113: p. 1379, 1959.
7. Khalatnikov, I. M., and Chernikova, D. M., *JETP*, Vol. 50: p. 411, 1966; English transl. *Soviet Physics–JETP*, Vol. 23: p. 274, 1966.
8. Disatnik, Y., to be published.

References (contd)

9. Lee, D. H., and Nicolet, M-A, "Space-Charge-Limited Currents in Solids for Various Geometries and Field-Dependent Mobility," *Solid State Electronics*, Vol. 8, pp. 182–184, 1965.

10. Nicolet, M-A., "Unipolar Space-Charge-Limited Current in Solids with Non-uniform Spacial Distribution of Shallow Traps," *J. Appl. Phys.*, Vol. 37, pp. 4224–4235, 1966.

11. Rose, A., "An Outline of Some Photoconductive Processes," *RCA Review*, Vol. 12, pp. 362–414, 1951.

12. Lampert, M. A., "Simplified Theory of Space-Charge-Limited Currents in an Insulator with Traps," *Phys. Rev.*, Vol. 103, pp. 1648–1656, 1956.

13. Lampert, M. A., "Volume-Controlled Current Injection in Insulators," *Rept. Progs. Phys.*, Vol. 27, pp. 329–367, 1964.

14. Shimada, K., "Theory of Thermionic Energy Conversion Part I. Surface Physics," Technical Memorandum 33-313, Jet Propulsion Laboratory, Pasadena, Calif., March 1, 1967.

15. Houston, J. M., "Measurement of Emitter Heat Balance in a Cesium Thermionic Converter," *Proceedings of the Thermionic Conversion Specialist Conference*, p. 214, October 1963.